Article:
Zotev, P.G., Wang, Y., Andres-Penares, D. et al. (2023) Van der Waals materials for applications in nanophotonics. Laser and Photonics Reviews, 17 (8). 2200957. ISSN: 1863-8880

https://doi.org/10.1002/lpor.202200957

LASER & PHOTONICS REVIEWS

www.lpr-journal.org

Van der Waals Materials for Applications in Nanophotonics

Panaiot G. Zotev, Yue Wang, Daniel Andres-Penares, Toby Severs-Millard, Sam Randerson, Xuerong Hu, Luca Sortino, Charalambos Louca, Mauro Brotons-Gisbert, Tahiyat Huq, Stefano Vezzoli, Riccardo Sapienza, Thomas F. Krauss, Brian D. Gerardot, and Alexander I. Tartakovskii**

Numerous optical phenomena and applications have been enabled by nanophotonic structures. Their current fabrication from high refractive index dielectrics, such as silicon (Si) or gallium phosphide (GaP), pose restricting fabrication challenges while metals, relying on plasmons and thus exhibiting high ohmic losses, limit the achievable applications. An emerging class of layered, so-called van der Waals (vdW), crystals is presented as a viable nanophotonics platform in this work. The dielectric response of 11 mechanically exfoliated thin-film (20–200 nm) vdW crystals is extracted, revealing high refractive indices up to $n = 5$, pronounced birefringence up to $\Delta n = 3$, sharp absorption resonances, and a range of transparency windows from ultraviolet to near-infrared. Nanoantennas are subsequently fabricated on silicon dioxide (SiO_2) and gold, utilizing the compatibility of vdW thin films with a variety of substrates. Pronounced Mie resonances are observed due to the high refractive index contrast on SiO_2, leading to a strong exciton-photon coupling regime as well as largely unexplored high-quality-factor, hybrid Mie-plasmon modes on gold. Additional vdW-material-specific degrees of freedom in fabrication are further demonstrated by realizing nanoantennas from stacked twisted crystalline thin-films, enabling control of nonlinear optical properties, and post-fabrication nanostructure transfer, important for nano-optics with sensitive materials.

1. Introduction

Nanophotonics in the 21st century has aimed to efficiently confine and manipulate light far below its wavelength using nanoscale structures. The motivation for fabricating these nanostructures lies in the applications enabled by their resonances in the visible and near-infrared portions of the electromagnetic spectrum including waveguiding in optical circuits,[1,2] Purcell enhancement of emission,[3–6] low-threshold lasing,[7] higher harmonic generation enhancement,[4,8] strong light-matter coupling,[9,10] and optical trapping.[11–13]

For more than a decade, this field of research largely focused on nanostructures fabricated from noble metals, which host plasmonic modes in nanoparticles,[9] nanoantennas,[14] waveguides,[15] and nanocubes.[16] While such metallic structures achieve vanishingly small mode volumes,[9] thereby increasing the light-matter interaction, they suffer from high ohmic losses,[17] cannot maintain magnetic resonances[18] and induce sample heating which may be detrimental for biological applications.[12] An alternative group of materials which provide solutions to these problems are dielectrics[19] such as silicon (Si),[3,12,18] germanium,[8] gallium arsenide (GaAs),[3,5] and gallium phosphide (GaP).[4,6]

Despite the many advances offered by traditional plasmonic and dielectric nanostructures, limitations in refractive index,

P. G. Zotev, T. Severs-Millard, S. Randerson, X. Hu, C. Louca, A. I. Tartakovskii
Department of Physics and Astronomy
University of Sheffield
Sheffield S3 7RH, UK
E-mail: p.zotev@sheffield.ac.uk; a.tartakovskii@sheffield.ac.uk

Y. Wang, T. F. Krauss
School of Physics, Engineering and Technology
University of York
York YO10 5DD, UK

D. Andres-Penares, M. Brotons-Gisbert, B. D. Gerardot
School of Engineering and Physical Sciences
Heriot-Watt University
Edinburgh EH14 4AS, UK

L. Sortino
Chair in Hybrid Nanosystems
Nanoinstitute Munich, Faculty of Physics
Ludwig-Maximilians-Universität
80539 Munich, Germany

T. Huq, S. Vezzoli, R. Sapienza
The Blackett Laboratory
Department of Physics
Imperial College London
London SW7 2BW, UK

The ORCID identification number(s) for the author(s) of this article can be found under https://doi.org/10.1002/lpor.202200957

DOI: 10.1002/lpor.202200957

fabrication difficulty, and versatility remain, yet can be resolved by the use of thin-film van der Waals materials. Similar to other dielectrics, layered materials do not suffer from ohmic losses, their nanostructures can maintain magnetic resonances[20] and do not induce detrimental sample heating. Due to the Moss rule concerning the inverse relation of the refractive index of dielectrics and their bandgap ($n \approx E_g^{-1/4}$),[21] the number of materials available for fabricating nanostructures without absorption in the visible range remain limited. Van der Waals materials can provide a solution as they offer larger refractive indices ($n > 4$) in this portion of the spectrum,[20,22] a range of transparency windows well into the ultraviolet[23] and numerous advantages due to their vdW adhesive nature to a variety of substrates without the necessity of lattice matching, a well known constraint of traditional dielectric nanophotonics.[24] Emerging from this, hybrid plasmonic-dielectric nanoresonators, yielding low optical losses and large photonic enhancement factors,[25] may become relatively simple to realize by transfer of a layered material onto a metallic surface followed by patterning of a nanophotonic structure. Another approach that is achievable due to the weak van der Waals adhesion is the fabrication of nanophotonic structures from stacked layers of the same or different materials with mutually twisted crystal axes which have applications in nonlinear optics.[26] This builds on previous work from the widely studied van der Waals heterostructure realizations[27] in which two monolayers were stacked in order to achieve different electronic or excitonic properties, such as interlayer excitons[28] and moiré superlattice effects,[29] in a hetero- or homobilayer. Additionally, post-fabrication techniques for designing bespoke nano-devices, such as repositioning via an atomic force microscope (AFM) tip[30] is readily available to vdW photonic structures, while not applicable to most structures made from traditional high refractive index dielectrics.

Recent works have demonstrated the fabrication of photonic crystal cavities, ring resonators, circular Bragg gratings, and waveguides from hexagonal boron nitride (hBN).[31] Nanoantennas,[20,30,32] photonic crystals,[33] microring resonators, and rib waveguides[34] as well as metasurfaces[34–37] have been fabricated from only two transition metal dichalcogenides (TMDs), namely tungsten diselenide (WS_2) and molybdenum disulfide (MoS_2). These structures have been used to demonstrate a range of applications including strong light-matter coupling,[20,33,35,36,38] waveguiding,[34,39] Purcell enhancement of emission,[30] and higher harmonic generation enhancement.[30,32,40,41] However, realizations of nanophotonic architectures using further vdW materials remain elusive despite numerical studies exploring exciting future applications in BICs[42] as well as entire optical circuits.[43]

In order to inspire and facilitate the use of a larger range of vdW materials for the fabrication of nanophotonic structures, in this work, we study the optical properties of a variety of layered materials and characterize their utility in different applications. The main advancements of our work are in the expansion of the layered materials toolkit available for nanophotonics and the demonstration of approaches for previously unattainable device design and fabrication which are fundamentally enabled by the use of van der Waals materials. The latter includes fabrication of hybrid metal-dielectric nanostructures, straightforward fabrication of thin-film twistable homo- and heterostructures suitable for photonics and also post-fabrication nanostructure transfer.

We begin by extracting the dielectric response of each material via micro-ellipsometry, yielding large refractive indices ($n > 4$) in the visible with a range of transparency windows from the near-infrared to the ultraviolet. We observe transparency in the out-of-plane orientation as well as large birefringence values ($\Delta n \approx 3$) for a number of layered materials.

We pattern single (monomer) and double (dimer) nanoantenna resonators into a range of vdW materials. Studying the resulting geometry of the nanoantennas provides insight into the etching selectivity of crystal axes in different materials. We also fabricate nanoantenna structures into twisted stacks of thin-film WS_2 crystals demonstrating an ability to fabricate nanophotonic homostructures in which optical properties, such as second harmonic generation (SHG), can be controlled via the twist angle.

The fabricated structures yield strong photonic resonances formed due to a large refractive index mismatch achievable as a result of the inherent ease of fabricating vdW structures on a silicon dioxide (SiO_2) substrate. This leads to the observation of strong light-matter coupling at room temperature exhibiting large Rabi splittings of >100 meV in single nanoantennas of different TMDs.

We subsequently demonstrate the versatility of vdW material nanofabrication by etching WS_2 monomer nanoantennas directly onto a gold substrate, realizing hybrid Mie-plasmonic resonances with high quality factors.[25] We also demonstrate the ability to recreate these nanostructures by employing a post-fabrication pick up and transfer technique, which we name "transferable photonics," useful for coupling nanoresonators to sensitive materials, such as TMD monolayers or biological systems.

As nonlinear light applications employing layered materials have drawn a significant interest in the past,[30,32,40,41] we further characterize the third order susceptibilities of several thin-film TMDs and demonstrate the application of third harmonic generation (THG) enhancement in WSe_2 nanoantennas.

2. Results

2.1. Linear Optical Properties of Van der Waals Materials

As a first step in characterizing vdW crystals for nanophotonics fabrication, we extract the refractive index and extinction coefficient of a number of popular materials including insulating hBN, TMDs, III–VI and magnetic materials. We begin by mechanically exfoliating multilayer crystals of 11 different vdW materials onto a 97 nm SiO_2 on Si substrate. We characterize the thickness of each crystal via AFM and measure the complex reflectance ratio of each sample via spectroscopic micro-ellipsometry, recording the amplitude (Ψ) and phase (Δ) at three different angles of incidence (AOI, see Note S1, Supporting Information), schematically shown in **Figure 1**a. Each set of data is fitted with an appropriate multilayer model yielding the real (n) and imaginary (κ) components of the complex refractive index shown in Figure 1b–l for each material including many members of the TMD family: WS_2, tungsten diselenide (WSe_2, MoS_2, molybdenum diselenide ($MoSe_2$), zirconium diselenide ($ZrSe_2$), hafnium

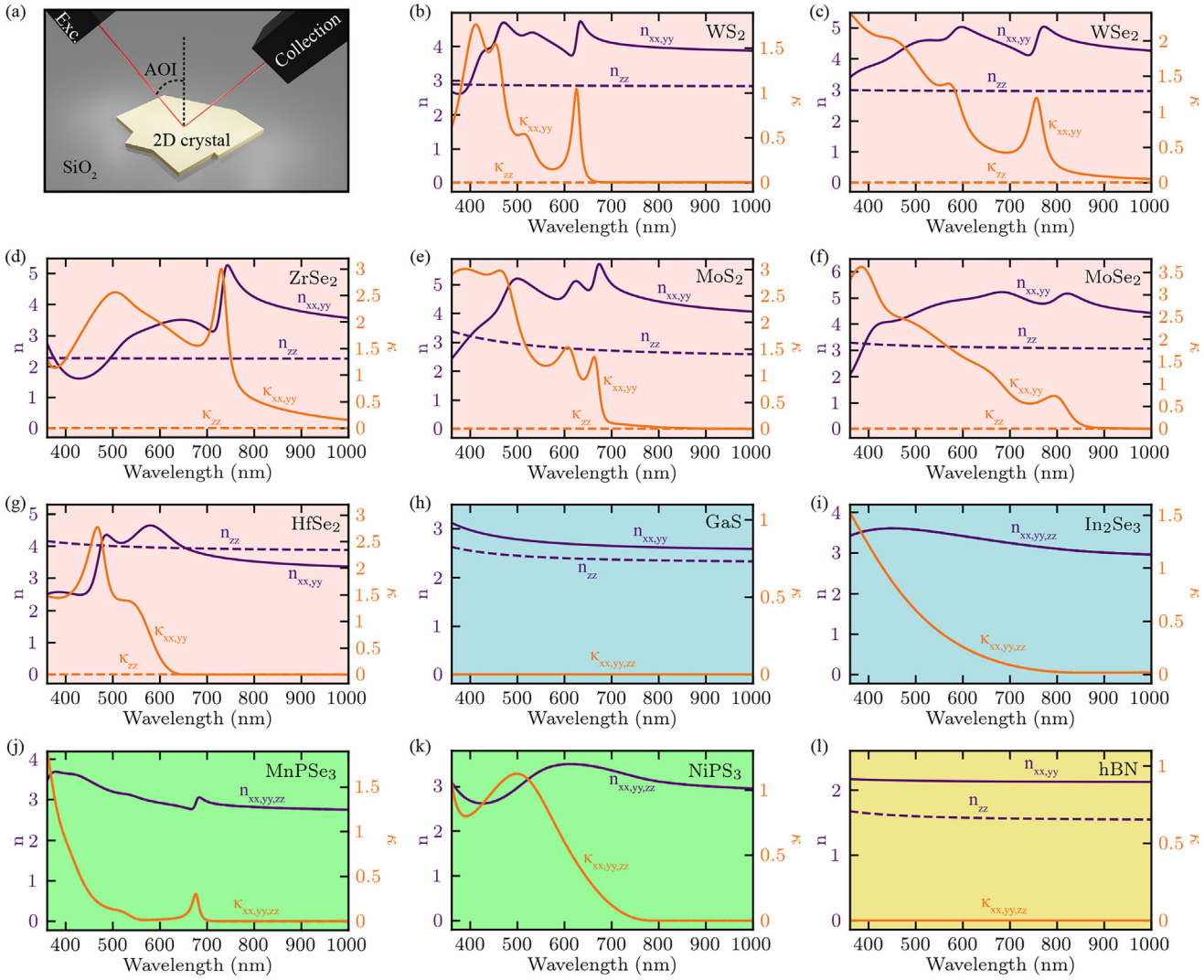

Figure 1. Refractive indices and extinction coefficients of layered materials a) Graphical representation of our micro-ellipsometry setup used to record the complex reflectance ratio from which we extract the dielectric response of each material. Refractive indices (n) and extinction coefficients (κ) extracted from ellipsometry measurements of the layered materials. These include TMDs (faint red background): b) WS_2, c) WSe_2, d) $ZrSe_2$, e) MoS_2, f) $MoSe_2$, and g) $HfSe_2$; III–VI materials (blue background): h) GaS and i) In_2Se_3; magnetic materials (green background): j) $MnPSe_3$ and k) $NiPS_3$; insulating (yellow background) l) hBN.

diselenide ($HfSe_2$), which are faintly shaded in red; two III–VI materials: gallium sulfide (GaS), indium selenide (In_2Se_3), which are shaded in blue; two magnetic layered materials: manganese phosphorus triselenide ($MnPSe_3$), nickel phosphorus trisulfide ($NiPS_3$), which are shaded in green; and the insulating hBN, which is shaded in yellow.

We use an analytical model appropriate to each material based on two considerations: the presence or absence of an absorption bandgap within the experimentally achievable wavelength range (360–1000 nm) and any anisotropy in the dielectric response due to crystallographic asymmetry. Therefore, we divided the 11 materials into three categories (see Note S1, Supporting Information) which are: semiconductors with a large bandgap (GaS, hBN), TMDs (WS_2, WSe_2, MoS_2, $MoSe_2$, $ZrSe_2$, $HfSe_2$) and isotropic materials (In_2Se_3, $MnPSe_3$, $NiPS_3$). We observe very strong absorption resonances, leading to high refractive indices, for well studied TMDs such as WS_2, WSe_2, MoS_2, and $MoSe_2$ which has been confirmed by previous reports in monolayers.[44] We also see prominent absorption resonances for $ZrSe_2$, $HfSe_2$, $MnPSe_3$, and $NiPS_3$ suggesting there may be a similar response in these materials. An interesting note here is that due to the strong binding energy of excitons in these materials, they are confined to individual layers and therefore, absorption processes can be ascribed to an in-plane regime while the out-of-plane regime remains transparent. This suggests that these materials are transparent for light propagating in-plane with an out-of-plane electric field. This anisotropy in the dielectric response results in especially high values of birefringence ($\Delta n \approx 3.0$) observed for MoS_2 and $ZrSe_2$ near their lowest energy excitonic resonances in near-infrared wavelengths (see Note S2, Supporting Information).

The extracted refractive indices and extinction coefficients for GaS, hBN, MoS_2, $MoSe_2$, WS_2, WSe_2, and In_2Se_3 are in good

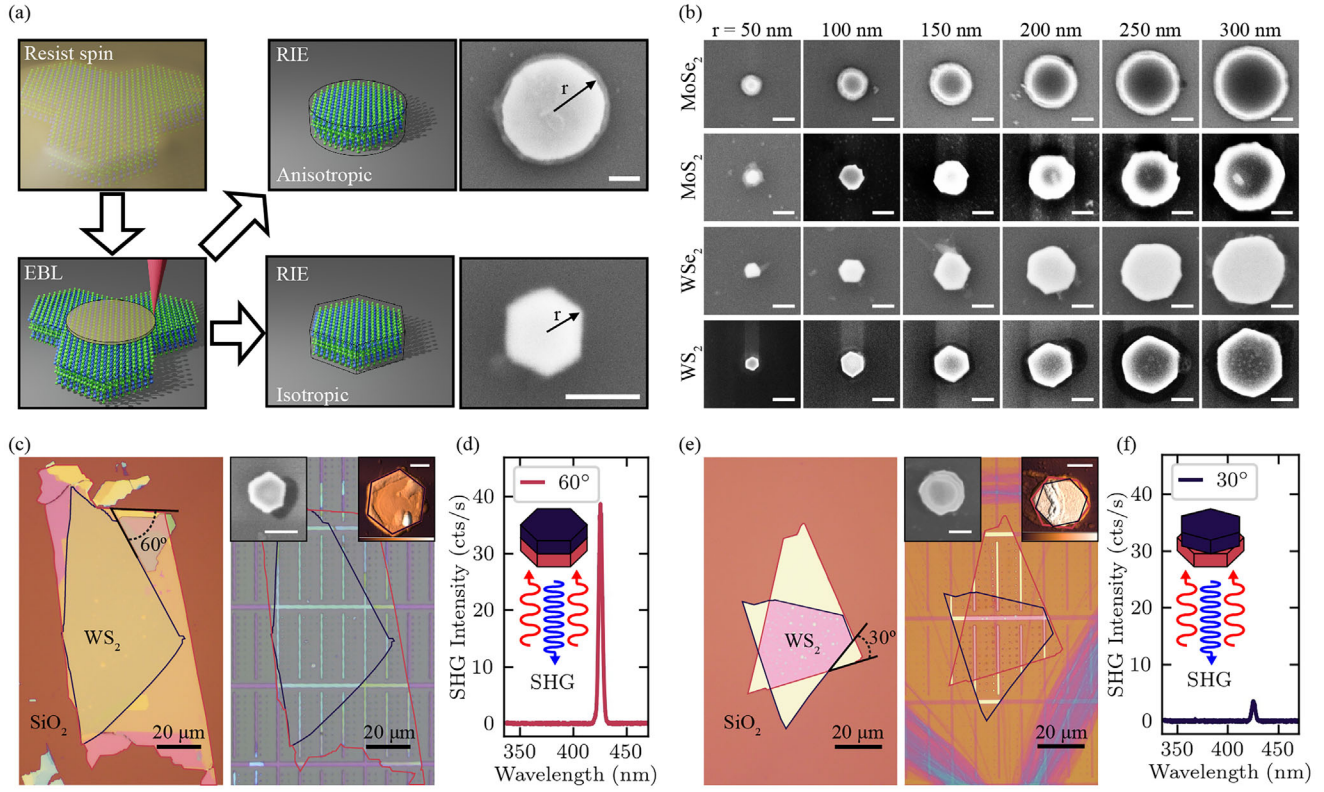

Figure 2. Fabrication of vdW material nanopillars. a) Fabrication steps and their order following the black outline arrows. The first step includes spinning of resist onto a vdW crystal. The second step is patterning and development after EBL into a circular geometry. The final step is RIE using either an anisotropic or isotropic etching recipe. The height (h) of the resulting nanostructure is defined by the thickness of the original thin-film. The radius (r) is defined as the distance from the center of the nanostructure to an outside vertex for the hexagonal geometry. b) Scanning electron microscopy (SEM) images of fabricated nanopillars in $MoSe_2$, MoS_2, WSe_2, WS_2 using the same isotropic etching recipe. WS_2 nanopillars maintain a hexagonal shape for all sizes while WSe_2 and MoS_2 exhibit circular geometries for a radius above 250 and 150 nm, respectively. Isotropic etching of $MoSe_2$ nanopillars maintain a circular shape for all recorded sizes. c) Optical images of a WS_2 homostructure achieved by the stacking of two thin-film crystals (thickness = 50 nm) with a 60° twist angle before (left panel) and after (right panel) fabrication of single nanopillars. The steps include the transfer of the crystals to form the homostructure on a SiO_2 substrate, EBL and RIE. Left inset: SEM image of a fabricated 60° twisted nanopillar. Right inset: AFM scan of a nanopillar in the 60° homostructure with hexagonal outlines to show the orientation of the top (black) and bottom (red) crystal. d) SHG spectrum collected from a 60° twisted nanopillar (r = 290 nm, h = 100 nm) under 850 nm laser excitation. e) Optical images of a WS_2 homostructure achieved by the stacking of two thin-film crystals (thickness = 30 nm) with a 30° twist angle before (left panel) and after (right panel) fabrication of single nanopillars. The fabrication steps are the same as for (c). Left inset: SEM image of a fabricated 30° twisted nanopillar. Right inset: AFM scan of a nanopillar in the 30° homostructure with hexagonal outlines to show the orientation of the top (black) and bottom (red) crystal. f) SHG spectrum collected from a 30° twisted nanopillar (r = 290 nm, h = 60 nm) under identical excitation as (d). All AFM and SEM scale bars = 200 nm.

agreement with previously reported values,[22,23,39,45–47] corroborating our approach. The extinction coefficients we extract for $HfSe_2$, $ZrSe_2$, and $NiPS_3$, which to the best of our knowledge have not been previously reported, are consistent with DFT calculations of absorption in $NiPS_3$,[48] $HfSe_2$, and $ZrSe_2$,[49] as well as experimentally measured absorption in $NiPS_3$.[50]

2.2. Nanoresonator Fabrication

In order to demonstrate the ease of fabrication of nanophotonic structures in layered materials, we pattern nanopillars into many of the optically studied crystals shown in Figure 1. After mechanical exfoliation of multilayered crystals of each material onto a nominally 290 nm SiO_2 on Si substrate, we spun a positive resist onto the sample and patterned it into arrays of disks with varying radii using electron beam lithography (EBL). After development, the resist pattern was transferred into the layered crystals via reactive ion etching (RIE, see Experimental Section) yielding monomer and dimer geometries with a high reproducibility in all of the fabricated nanostructures (see Note S3, Supporting Information). **Figure 2**a displays a schematic representation of the fabrication process which results in differing geometries in some TMDs, namely circular and hexagonal, as a result of an anisotropic and isotropic etch, respectively. This is due to etch selectivity in the armchair as opposed to the zigzag crystal axis.[30,34,51,52]

It may be expected that all TMDs will result in similar geometries after an isotropic fabrication procedure due to their identical crystal symmetry, however, this is not observed as shown in Figure 2b. For a small nanopillar radius of r = 50 nm, WS_2, WSe_2, and MoS_2 result in a hexagonal geometry, however, this is not true

for $MoSe_2$ which yields a circular geometry. For larger nanopillar radii, most of the materials also result in a circular geometry with the exception of WS_2 which maintains a hexagonal shape up to a radius of 300 nm. The transition from hexagonal to circular geometry can be seen at a radius of 150 nm for MoS_2 and 250 nm for WSe_2. As these crystals have undergone the same etching conditions for the same amount of time, this suggests that ionized fluorine radicals react with and remove some materials faster than others, leading to a hexagonal geometry in larger structures of certain TMDs.[52] This is supported by theoretical calculations and experimental results for the enthalpy of formation of each material: -120.2 kJ mol^{-1}(WS_2,[53]), −185.3 kJ mol^{-1}(WSe_2,[54]), −234.2 kJ mol^{-1}($MoSe_2$,[55]), −271.8 kJ mol^{-1}(MoS_2,[54]), where the increasingly negative values indicate a more stable material. Thus, the less negative values suggest that dissociation of materials such as WS_2 and WSe_2 requires less energy than MoS_2 and $MoSe_2$. An additional contribution to the formation of a hexagonal geometry is the crystal thickness of each of the etched materials, which are as follows: 43 nm (WS_2), 85 nm (WSe_2), 78 nm (MoS_2) and 29 nm ($MoSe_2$). A smaller thickness leads to less surface area for etching in plane and thus results in less hexagonal nanopillars. These two contributions of the crystal thickness and the enthalpy of formation suggest relative etching speeds of TMD materials which can be ranked as: $WS_2 > WSe_2 > MoS_2 \approx MoSe_2$.

Fabrication of hBN and $HfSe_2$ nanopillars yields a circular geometry regardless of which previously employed etching recipes was used (see Supporting Note S3, Supporting Information) suggesting low or no crystal axis selectivity. Nanopillars in GaS also yield a circular geometry (see Note S3, Supporting Information), although, the etching step was changed to employ a chlorine gas due to the poor reactivity of fluorine radicals with this material (see Experimental Section). Similar to WS_2, fabrication of $ZrSe_2$ can yield both circular and hexagonal geometries up to a radius of 400 nm depending on the etching recipe used (see Note S3, Supporting Information) suggesting a similarly fast etching speed and low enthalpy of formation. Subsequent attempts to etch In_2Se_3, $NiPS_3$, and $MnPSe_3$ with all etching recipes involving fluorine and chlorine gases yielded a very poor etch rate which did not form any appreciable nanostructures in the thin-film crystals (see Note S3, Supporting Information). Different methods of etching involving non-reactive ion sputtering, focused ion beam milling or wet etching may yield more satisfactory results, however, this is beyond the scope of this work.

In order to demonstrate the fabrication possibilities enabled by using vdW materials for nanophotonics, we also etched single nanopillars into twisted homostructures achieved by the stacking of two WS_2 thin-film crystals via an all-dry transfer technique (see Experimental Section) available only to layered dielectrics. As a general rule, this includes all of the materials which we have studied and any semiconducting materials which can be mechanically exfoliated. This homostructure fabrication is an extension of the technique used to fabricate hetero- and homobilayers[27–29] which has so far not been applied in a photonic structure context, thus realizing nanostructures which could not previously be designed.

We fabricated nanopillars into two homostructures each of which consisted of two thin-film crystals stacked at 60° and 30° twist angles on SiO_2 substrates as shown in the left panels of Figure 2c,e, respectively. The thickness of the constituent crystals used in the fabrication of the homostructures was 50 and 30 nm for the 60° and 30° twist angle samples, respectively. Utilizing EBL pattering and isotropic etching, we obtained single nanopillars with heights of 100 and 60 nm for the 60° and 30° twisted homostructures as shown in the right panels of Figure 2c,e respectively. As the crystal axes of each constituent thin-film in the homostructure are rotated with respect to each other due to the twist angle, the isotropic etching step will result in a rotated hexagonal structure for each. This rotation is not visible in the nanopillars of the 60° sample, shown in the insets of the right panel of Figure 2c, as the twist angle will yield hexagonal structures which form directly above each other. However, the 30° twist angle is visible in the nanopillars fabricated from the other homostructure shown in the insets of the right panel of Figure 2e as this yields hexagonal structures with a 30° rotation. The twist angle in an unetched portion of the crystal was confirmed with SHG experiments, which yielded a brighter signal from the 60° homostructure when compared to the 30° sample (see Note S4, Supporting Information). This result is expected as the thickness of the WS_2 homostructures was far below the coherence length of the SHG signal in this material and the centrosymmetry at the interface between the two constituent crystals was increasingly broken with twist angle.[26] This same bright SHG signal was also observed for 60° nanopillar structures as opposed to those fabricated in the 30° homostructures ($r = 290$ nm for both homostructures) as shown by the spectra plotted in Figure 2d,f. This confirms that the broken centrosymmetry of the interface is consistent for both the unetched crystal and nanopillar structures as no additional enhancement is expected from photonic resonances.

2.3. Photonic Resonances of Fabricated Nanoantennas

We subsequently studied the fabricated single and double nanopillar structures from a range of these materials using dark field spectroscopy. The height, radius, and dimer separation gap were measured using AFM and SEM techniques. **Figure 3**a–d shows the dark field spectra of monomer nanopillars over a range of radii for different layered materials including MoS_2 ($h = 70$ nm), $MoSe_2$ ($h = 35$ nm), WSe_2 ($h = 85$ nm), and GaS ($h = 200$ nm). When compared with simulations of the scattering cross section expected for these nanostructures, we observed close agreement enabling us to identify neutral excitonic absorption in the material (X^0), geometric Mie resonances such as magnetic dipole (MD), electric dipole (ED), magnetic quadrupole (MQ), and electric quadrupole (EQ) resonances as well as light-confining anapole (AM) and higher order anapole (HOAM) modes (see Note S5, Supporting Information). Similarly, we also measured the dark field spectra of dimers in MoS_2 ($h = 190$ nm), $MoSe_2$ ($h = 30$ nm), WSe_2 ($h = 45$ nm), and GaS ($h = 145$ nm) with gaps ranging from 50 to 200 nm, shown in Figure 3e–h and compared these to simulations (see Note S5, Supporting Information) which also agreed well, demonstrating the possibility of realizing more complex nanophotonic architectures. Additionally we have measured the dark field spectra of monomers and dimers fabricated from WS_2 and hBN which also yield similar resonances (see Note S6, Supporting Information). For GaS and hBN, we observe the formation of resonances at near-ultraviolet wavelengths due to the lack of absorption in these

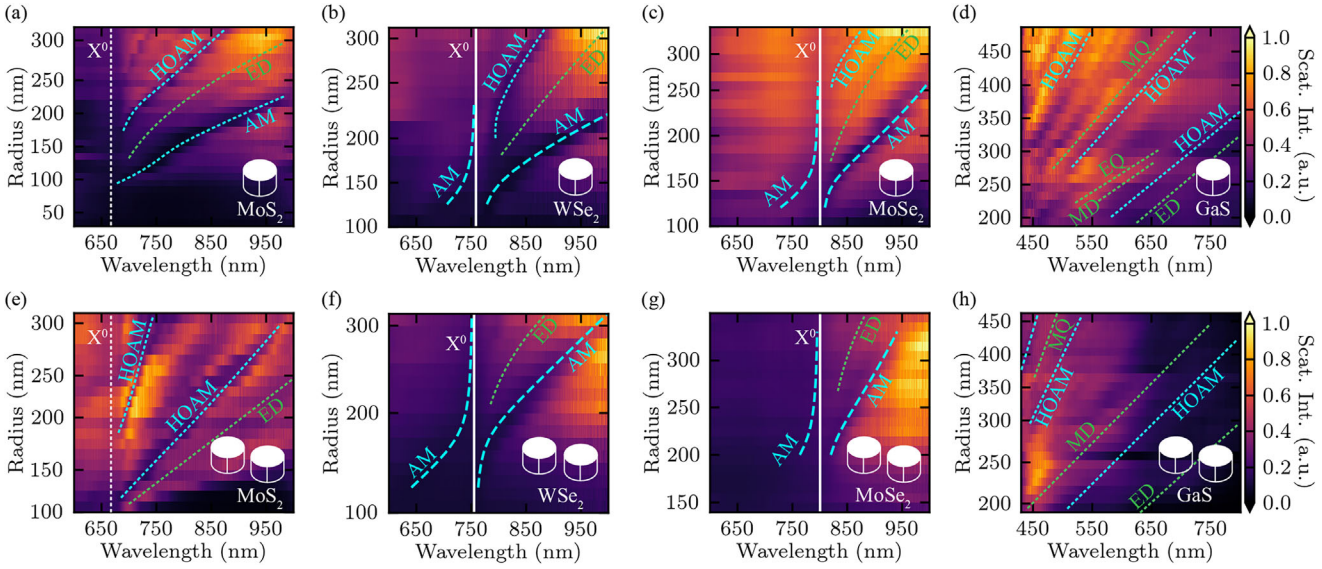

Figure 3. Dark field spectra of monomer and dimer nanoantenna resonances in a variety of vdW materials. a–d) Experimental dark field spectra for monomer nanoantennas with a range of radii in MoS_2 ($h = 70$ nm), WSe_2 ($h = 85$ nm), $MoSe_2$ ($h = 35$ nm), and GaS ($h = 200$ nm). Identified resonances include the neutral exciton resonance of the material (X^0, white), the magnetic dipole (MD, green), electric dipole (ED), magnetic quadrupole (MQ), and electric quadrupole (EQ) resonances as well as the anapole mode (AM, cyan) and higher order anapole mode (HOAM). e–h) Experimental dark field spectra for dimer nanoantennas with a range of radii in MoS_2 ($h = 190$ nm), WSe_2 ($h = 45$ nm), $MoSe_2$ ($h = 30$ nm), and GaS ($h = 145$ nm). Dimer gaps range from 50 to 200 nm. Identified resonances are similar to those in monomer nanoantennas.

materials. We also observe a multitude of higher-order peaks in the dark field spectra of GaS monomer nanoantennas which are a result of a superposition of multiple Mie resonances, such as a magnetic and electric quadrupole as well as an electric dipole mode. Due to fabrication imperfections, some of the peaks are more or less prominent in the experimental than the simulated spectra. The stability of the fabricated nanostructures in ambient conditions and its impact on their photonic performance is also noteworthy. In order to asses this, we measure the dark field spectra of WS_2, MoS_2, and hBN monomer nanoantennas as well as the lateral size of GaS and $HfSe_2$ nanopillars after a period of storage in ambient conditions (see Note S7, Supporting Information). We observe no noticeable shifts in the resonances or changes in the geometry of any of the fabricated structures, vital for Mie resonances, from 8 to 18 months after their fabrication suggesting stable optical performance for all vdW material nanophotonic structures.

The WS_2 twisted homostructure monomers shown in Figure 2c,e also yielded Mie and anapole resonances (see Note S4, Supporting Information) confirming them to be nanoantennas. Additionally, we observe that the twist angle does not change the electronic properties of the materials, seen in the position of the neutral exciton resonance in the dark field spectra plotted in Note S4, Supporting Information. Thus, the introduction of a twist angle does not alter the refractive index of the material, yet enables nanophotonic device designs which are not possible with traditional materials.

Focusing solely on the TMDs, we observe an anticrossing of the anapole modes with the neutral exciton for nanoantenna radii at which the energies of these two are expected to be degenerate providing evidence of strong light-matter coupling. As absorption is high at wavelengths below that of the X^0, the higher order anapole resonance is not as clearly defined in this range and its signature minimum is not clearly visible in the data limiting our ability to fit this. We have, however, fitted the anticrossing of the anapole mode with the neutral exciton for WSe_2 and $MoSe_2$ monomers using a coupled oscillator model. We extracted an energy splitting of 141 meV for WSe_2 monomers ($r = 120$ nm, $h = 85$ nm) as well as 100 meV for $MoSe_2$ monomers ($r = 135$ nm, $h = 35$ nm). Using a previously reported condition which indicates that the coupling strength of the exciton and photon resonances must be larger than the average of the individual linewidths[56,57] (see Note S5, Supporting Information), the measured energy splittings in WSe_2 and $MoSe_2$ monomers were confirmed to be evidence of strong light-matter coupling. A similar anticrossing was observed for dimer structures in WSe_2 (132 meV for $r = 155$ nm, $h = 45$ nm), $MoSe_2$ (104 meV for $r = 215$ nm, $h = 30$ nm) and WS_2 (153 meV for $r = 130$ nm, $h = 40$ nm, see Note S6, Supporting Information). However, due to the larger linewidths of the neutral exciton and anapole resonances in these structures, the anticrossings do not satisfy the strong coupling condition instead indicating intermediate coupling by satisfying a complementary condition $(\Omega_R > (\frac{1}{\gamma_{X^0}} - \frac{1}{\gamma_{AM}})/2)$.[57] FDTD simulations also confirm the strong and intermediate coupling between excitons and anapole modes yielding expected Rabi splittings as high as 200 meV for WSe_2 monomers and 179 meV for WS_2 dimers. Additionally, a higher order anapole mode is also observed to strongly couple to the exciton in simulations yielding Rabi splittings as high as 210 meV for WS_2 monomers. Smaller experimental anticrossings were also observed for monomer nanoantennas fabricated from WS_2 (see Note S6, Supporting Information) and MoS_2, which was limited due fabrication imperfections in these nanostructures as well as large absorption at wavelengths below

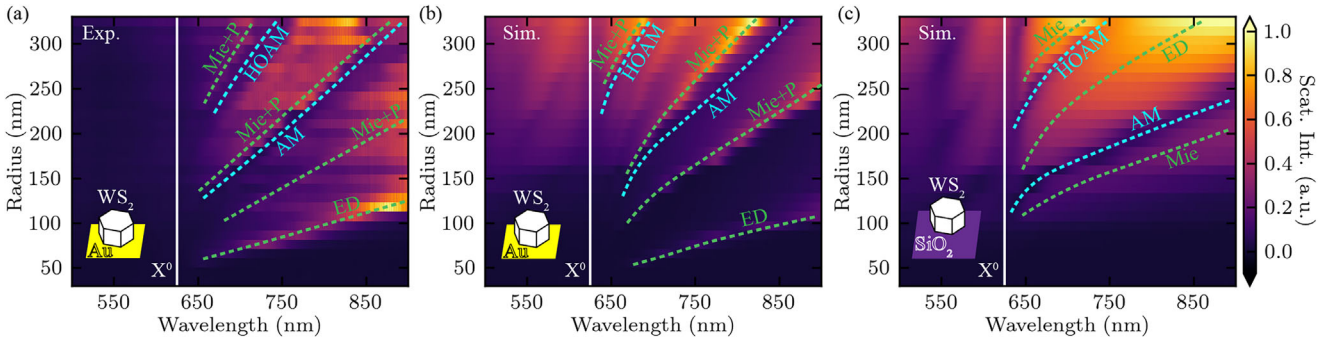

Figure 4. Experimental and simulated dark field spectra of WS_2 hexagonal monomer nanoantennas on different substrates. a) Experimental dark field spectra of WS_2 hexagonal monomer nanoantennas ($h = 62$ nm) with a range of radii fabricated onto a susbrate with a 130 nm thick gold film. Identified resonances include the neutral exciton resonance of WS_2 (X^0, white solid line), Mie resonances such as the electric dipole (ED), magnetic quadrupole, and electric quadrupole resonances hybridized with a plasmonic component (Mie+P, green dashed curves) as well as the anapole mode (AM, cyan dashed curves) and higher order anapole mode (HOAM). b) Simulated scattering intensity of WS_2 hexagonal monomer nanoantennas with the same height and range of radii as in (a) on a semi-infinite gold substrate showing close agreement to the experimental results. Identified resonances are the same as those shown in (a). c) Simulated scattering intensity of WS_2 hexagonal monomer nanoantennas with the same height and range of radii as in (a) on a semi-infinite SiO_2 substrate displaying broadened resonances. Identified resonances include similar yet broadened Mie as well as anapole and higher order anapole modes.

the neutral exciton resonance limiting our ability to accurately fit these features. Additionally, due to the strong dependence of the exciton energy[58] and the weak dependence of the photonic resonance wavelength on temperature, heating or cooling of the nanoantennas can be employed to tune the spectrum of the anticrossings and thus shift the energy at which we observe strong coupling. Temperature tuning may also prove useful for fine control of the spectral overlap between emitters and photonic resonances in Purcell enhancement applications[59] due to only subtle changes in the refractive index of these materials.[58]

2.4. Dielectric Nanoantennas on a Metallic Substrate

We have demonstrated that the fabrication of vdW nanoresonators on a low refractive index substrate such as SiO_2 is possible and results in well formed resonances in structures with heights as low as 30 nm. While this large index mismatch between substrate and nanoantenna may lead to tightly confined resonances, it can be advantageous to fabricate dielectric nanostructures onto a reflective substrate such as a gold mirror. This is expected to enable very high Q factor (10^3) hybrid dielectric-plasmonic modes which can provide very large Purcell factors (>5000).[25] It is reasonable to expect that all van der Waals materials which have been studied in this work, as well as any that are mechanically exfoliated, can be deterministically deposited onto arbitrary surfaces including SiO_2 and gold. We thus proceed to fabricate an array of WS_2 monomer nanoantennas directly on a substrate with a 130 nm gold film. After exfoliation directly on the gold, similar to the technique used for a SiO_2/Si substrate, EBL and RIE is used to define WS_2 monomer nanoantennas with a circular and hexagonal geometry using the previously described recipes. An additional benefit to fabricating nanostructures in vdW materials onto a gold substrate arises due to the low etch rate of the gold compared to the previously used SiO_2. This forms a natural etch stop which allows for a higher tolerance in fabrication errors concerning the etch rate and time.

We subsequently record the dark field spectra of an array of the fabricated hexagonal WS_2 monomer nanoantennas on gold, plotted in **Figure 4**a. After characterization of the height ($h = 62$ nm) and radii of the nanoantennas using AFM and SEM, respectively, we simulate the expected scattering intensity, shown in Figure 4b and observe close agreement with experiment. This allows us to identify Mie and anapole modes similar to those found in the nanostructures fabricated on SiO_2.

In order to compare these structures to those previously fabricated on a low refractive index substrate, we also simulate the scattering intensities of identical WS_2 hexagonal monomer nanoantennas onto a SiO_2 substrate, displayed in Figure 4c. Similar resonances are identified in these nanostructures, however, we observe a blueshifted ED mode and redshifted anapole modes which appear broader than those recorded for a gold substrate. For larger radii, we observe the appearance of additional modes in the nanoantennas fabricated on a gold substrate which we attribute to the formation of hybrid Mie-plasmonic (Mie+P) resonances. A plasmonic contribution may also be present for smaller nanoantenna radii, hybridizing with and enhancing spectral features which we identified as dielectric Mie (ED) and anapole resonances[25] due to mirror charge currents in the gold which respond to the induced bound charge currents in the WS_2 nanoantennas. The reduced broadening of resonances in the nanostructures fabricated on gold leads us to consider the confinement of the electric field inside and in close proximity to the nanoantenna structure. Electric field intensity profiles recorded in and surrounding a WS_2 monomer nanoantenna at the anapole and electric dipole modes for a gold and SiO_2 substrate reveal differing confinements, shedding light on the origin of the mode shift, as well as increased intensities on the metallic substrate by at least an order of magnitude (see Note S8, Supporting Information). These suggest that the contribution of plasmonic resonances to the observed features in scattering may not be negligible.

Additionally, we compare the quality factors of the identified ED resonance in monomer nanoantennas fabricated from

Table 1. Experimental and simulated quality factors for Mie resonators. The quality factors were extracted from Lorentzian fits to experimental and simulated electric dipole resonances in different materials on different substrates. Values were extracted for resonators from this work as well as previous reports of monomer nanoantennas. Black and orange numbers represent quality factors extracted for monomer nanoantennas on a dielectric and gold substrate, respectively..

Materials	WS_2	WSe_2	MoS_2	$MoSe_2$	GaS	Si[60]	GaAs/AlGaAs[61]
Exp. ED Q	4.95 (12.64)	4.66	4.04	4.03	5.21	7.04	
Sim. ED Q	3.99 (14.27)	6.58 (11.72)	4.63 (14.94)	5.36 (17.98)	5.26 (6.11)		4.60

different vdW materials on a gold and SiO_2 substrate both in simulation and experiment as shown by **Table 1**. The ED resonance was chosen as it was observed in all of the experimentally studied nanoantennas and leads to a high outcoupling of emitted light, which is important for most nanophotonic applications. The black and orange numbers correspond to a SiO_2 and gold substrate, respectively. Each value was extracted from a Lorentzian fit of a resonance peak in scattering for a monomer nanoantenna geometry yielding a mode far from any anticrossings. For all materials, the extracted quality factors of resonances in nanostructures on a gold substrate yield higher values than for a SiO_2 substrate in both experiment and simulation as suggested by the large reduction in broadening observed in Figure 4a,b when compared to Figure 4c. Previously reported Mie resonances in dielectric monomer nanoantennas[60,61] also yield lower quality factors than observed in our vdW nanoantennas on gold. These results suggest that the hybridization of Mie and plasmonic resonances may provide a large contribution to the quality factor enhancement.

Some applications may require the placement of nanophotonic structures onto substrates which can be damaged by standard nanofabrication techniques such as biological samples[12] or substrates with deposited monolayer TMDs. We show that the nanoantennas we fabricate can be transferred onto such sensitive surfaces by taking advantage of their weak van der Waals adhesion to the substrate. Note S9 in the Supporting Information shows the transfer of WS_2 hexagonal nanoantennas onto a monolayer and bilayer WSe_2 crystal which has been previously deposited onto a gold substrate. This regime of nanostructure fabrication, which we name "transferable photonics," enables the formation of tightly confined hotspots which can provide many orders of magnitude enhancement to emission sources, previously demonstrated for plasmonic structures,[9] as well as applications which contain sensitive samples that may be damaged by standard nanofabrication techniques. Further development of this method is required in order to achieve a more controlled pick up and transfer of the nanostructures, which may prove easier for other resonators such as photonic crystal cavities or metasurfaces,[62] however, this is beyond the scope of this work.

2.5. Nonlinear Optical Properties and Applications

As there is a large interest in employing vdW materials for enhancing nonlinear light applications,[30,32,37,40,41] we assess the viability of the most widely used TMDs for higher harmonic generation by exciting several thin-film crystals from each material with 220 fs laser pulses, nominally centered at 1500 nm. **Figure 5**a displays the THG spectrum from a WSe_2 thin-film crystal. The THG signal is observed at 498 nm (as the excitation has drifted to 1494 nm), with a small shoulder that we attribute to the laser spectrum, which also exhibits this feature. We observe a strong THG signal from this and other TMD materials and thus we extract the third harmonic susceptibility ($\chi^{(3)}$) for each by comparing our recorded THG intensity with nonlinear scattering theory[63] coupled with transfer-matrix method simulations (see Note S10, Supporting Information). The extracted $\chi^{(3)}$ values are plotted in Figure 5b where the error bars indicate the uncertainty in the measurement of the thickness of each thin-film crystal via AFM. The third harmonic susceptibilities we extract are up to an order of magnitude higher than for monolayers of the same material,[64–66] which is expected due to the difference in nonlinear properties between monolayer and multilayer crystals as well as the strong thickness dependence of the model used to to extract the $\chi^{(3)}$ values. These values are also up to four orders of magnitude larger than in BBO crystals regularly used for laser frequency tripling.[67] We observe the highest third harmonic susceptibility in MoS_2 and the lowest in $MoSe_2$.

Next, we pattern monomer nanoantennas with varying radii (r = 200–280 nm) into a WSe_2 crystal with 250 nm thickness. An SEM image of the fabricated array is displayed in Figure 5c. We record the dark field spectra of the nanoantennas in the visible range and compare these to simulations including both visible and near-infrared wavelengths which are in good agreement as shown in Figure 5e. From the simulated infrared scattering intensity we observed an anapole mode scattering minimum redshifting from 1200 to 1600 nm with increasing nanoantenna radius, which can be used for enhancing higher harmonic generation. Thus, we illuminate the nanoantennas with a laser at a wavelength of 1400 nm and reposition our excitation and collection spot across the array of nanoantennas in order to record a map of the THG signal (see Experimental Section). As shown in Figure 5d, the THG signal is maximized at the position of certain nanoantennas (r = 240 nm) as opposed to others indicating a resonant coupling of the excitation laser leading to higher third harmonic signal. The nanoantennas which exhibit the brightest THG signal at 1400 nm illumination also exhibit an anapole mode minimum near this wavelength, as shown in Figure 5e, providing further evidence for coupling of the excitation to the resonance of the nanoantenna. We subsequently vary the wavelength of the illumination source and observe the maximum THG signal shift from lower radius nanoantennas to those with a higher radius for an increasing excitation wavelength as shown in Figure 5f thereby confirming that the excitation is coupling to the anapole mode in the WSe_2 monomer nanoantennas.

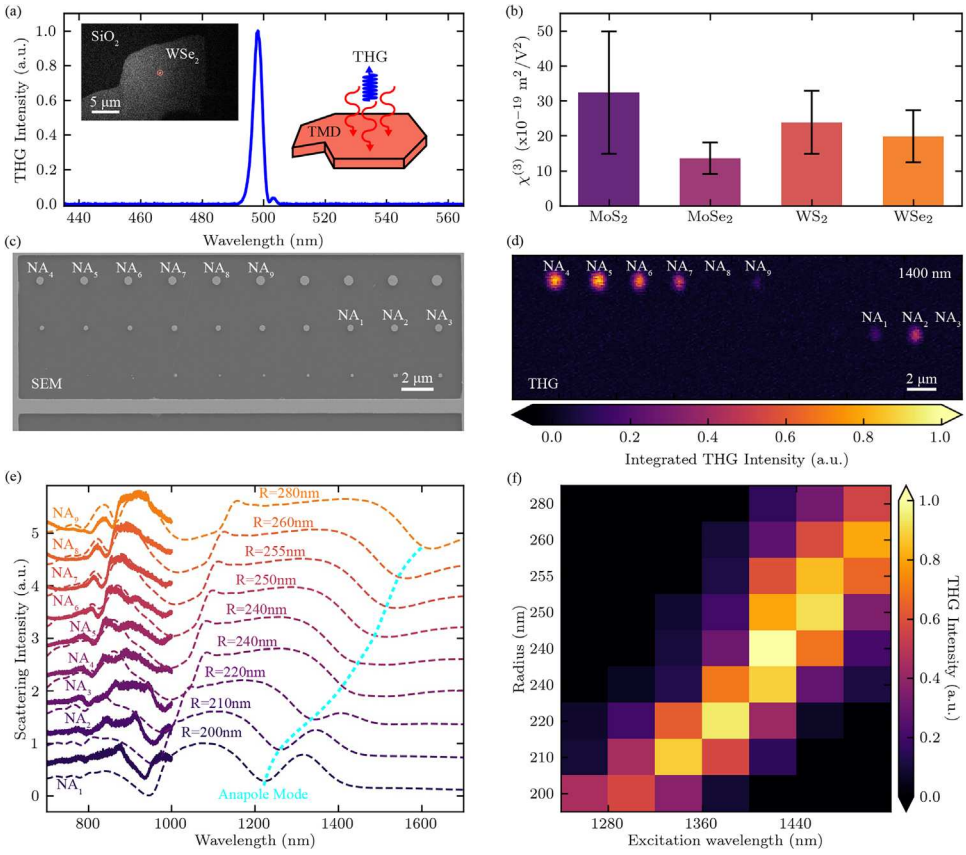

Figure 5. THG experiments with TMDs. a) Third harmonic generation spectrum from WSe_2 thin-film crystal under 1494 nm excitation. Left inset: Optical image of a WSe_2 crystal under study. Right inset: Schematic of THG from TMD crystals. b) Third harmonic susceptibilities ($\chi^{(3)}$) extracted for different TMD crystals for 1500 nm excitation. The error bars show the error in measurements of the thickness via AFM. c) SEM image of array of WSe_2 monomers under study with labels for the nanoantennas of interest. d) Map of the THG signal across the array shown in (c) under 1400 nm excitation. Nanoantennas NA_4 and NA_5 exhibit the brightest THG signal for this wavelength of illumination. e) Experimental dark field spectrum of each monomer nanoantenna compared with simulations of the scattering cross section of each geometry. The formation of an anapole mode, which can be used for THG enhancement, is highlighted. f) THG signal intensity from each nanoantenna under a range of excitation wavelengths. A resonant enhancement is observed at larger nanoantennas for increasing excitation wavelengths as expected from the redshifting anapole mode to which the THG signal is coupled.

3. Discussion

We have studied a range of different vdW materials for their potential use as nanophotonic structures and demonstrated their advantages compared to traditional dielectric or plasmonic materials. We extract the dielectric response of 11 different layered materials via micro-ellipsometry. We observe very high refractive indices ($n > 5$ for some materials) when compared to Si or GaAs ($n \approx 4$[68]) as well as a range of transparency windows from ultraviolet to near-infrared wavelengths. Utilizing material specific fitting models to extract the linear optical parameters leads to very high values of birefringence ($\Delta n \approx 3.0$) in MoS_2 and $ZrSe_2$ as well as transparency for light propagating in-plane with an out-of-plane electric field in WS_2, WSe_2, MoS_2, $MoSe_2$, $ZrSe_2$, $HfSe_2$, GaS, and hBN.

We fabricate nanoantenna structures in widely used vdW materials (MoS_2, $MoSe_2$, WS_2, WSe_2, hBN, $HfSe_2$, $ZrSe_2$, and GaS). The geometries of nanostructures undergoing the same isotropic fabrication conditions provide insight into the etching speed and selectivity of some TMDs which can be ranked as: $ZrSe_2 \approx WS_2 > WSe_2 > MoSe_2 \approx MoS_2$. Etching of In_2Se_3, $MnPSe_3$, and $NiPS_3$ nanoantennas is beyond the scope of this work, however, our attempts with fluorine and chlorine gasses using both isotropic and anisotropic conditions indicate that other RIE or wet etching approaches may be necessary. Nanoantenna fabrication in $MnPSe_3$ and $NiPS_3$ may lead to optical control of the magnetic properties of these materials via coupling to a magnetic dipole mode. Additionally, our demonstration of monomer nanoantennas in twisted WS_2 thin-film homostructures provides a straightforward route for future fabrication of heterostructure nanophotonic resonators such as 3D photonic crystal cavities or moiré architectures[69] with integrated emissive materials, such as monolayer TMDs, enabled by the the weak van der Waals adhesion of layered dielectrics. The twist angle does not change the electronic and excitonic properties or the refractive index of the nanostructure material in this context, yet enables nanophotonic device designs which are not possible with previously used materials. The SHG signal observed from the interface of the twisted WS_2 homostructure, with a thickness far below the coherence length in this material, can be enhanced due to coupling with the

anapole mode in nanoantennas and may provide insights into interlayer excitons in multilayer TMD crystals.

Dark field spectroscopy of the fabricated structures in MoS_2, $MoSe_2$, WS_2, WS_2 twisted homostructures, WSe_2, GaS, and hBN on SiO_2 results in well defined Mie and anapole resonances from ultra-violet to near-infrared wavelengths. The fabricated nanostructures also yield a stable optical performance many months after fabrication. Strong coupling within single nanostructure was observed at room temperature in several TMD crystals with extracted Rabi splittings as high as 153 meV for WS_2, 141 meV for WSe_2, and 104 meV for $MoSe_2$ nanoantennas. This is a factor of five larger than reported for monolayer TMDs in high Q microcavities[70,71] and one to two orders of magnitude higher than in InGaAs,[72] AlGaAs[73,74] and AlGaN[75] multiple quantum wells in similar microcavities. An additional tuning mechanism is also available to control the spectral position of the observed strong coupling using temperature. This mechanism is also useful for fine tuning of the spectral overlap of emitters and photonic resonances in Purcell enhancement applications.[59]

Evidence of the possibility of fabricating vdW nanostructures on virtually any substrate without the need for lattice matching is provided by the patterning of nanoantennas onto a SiO_2 as well as gold substrate. This provides the possibility for straightforward realization of large refractive index contrast interfaces as well as the integration of dielectric and plasmonic nanophotonic devices.[25] The fabricated WS_2 nanoantennas on gold yield highly confined resonances with improved Q factors which may be beneficial for a number of applications including Purcell enhancement of emission, quantum efficiency enhancement,[25] collection efficiency enhancement, strong light matter coupling, optical trapping, and surface enhanced Raman spectroscopy among others. Additional possibilities, demonstrated by our deposition of pre-fabricated WS_2 nanoantennas onto a WSe_2 monolayer on a gold substrate, include the transfer of etched nanostructures from one substrate onto another which contains sensitive samples such as monolayer TMDs or biological samples.

We also characterize the nonlinear optical properties of some of the most widely studied vdW crystals by extracting the THG susceptibility of various thin-film TMDs near the telecom C band, advantageous for quantum applications,[76] yielding values up to an order of magnitude higher than in monolayers[64–66] and up to four orders of magnitude larger than in BBO crystals regularly used for laser frequency tripling applications.[67] We also explore a method of enhancing such nonlinear signals via coupling to resonances in monomer nanoantennas of WSe_2.

Due to their high refractive indices, wide range of bandgaps and adhesive properties, vdW material nanostructures enable a wide variety of applications as shown by our demonstrations of twisted homostructure nanoresonators, single nanoantenna strong coupling, hybrid high-Q Mie-Plasmonic modes, post-fabrication nanostructure deposition and THG enhancement. The advantages of using van der Waals materials will enable many exciting opportunities in nanophotonics.

4. Experimental Section

Ellipsometry: Spectroscopic ellipsometry measurements were carried out in the wavelength range 360 to 1000 nm with a spatial resolution of $\approx 1\ \mu m^2$ using a nulling imaging ellipsometer (EP4, Accurion Gmbh) in an inert Ar atmosphere at room temperature. Ellipsometric data from the samples were acquired at three different AOI (defining the vertical as AOI = 0°) at 45°, 50°, and 55°.

Van der Waals Materials Exfoliation: Layered material crystals were mechanically exfoliated from bulk (HQ-graphene) onto a nominally 290 nm SiO_2 on Si or gold substrate. Large crystals with recognizable axes via straight edged sides at 120° to each other were identified and their positions within the sample were recorded for further patterning.

Homostructure Fabrication: The 60° and 30° stacked homostructures were fabricated with an all dry transfer technique. For the 60° homostructure, two separate 50 nm WS_2 crystals were exfoliated onto a PPC/SiO_2 substrate. These were then picked up consecutively with a 60° twist angle using a PMMA/PDMS membrane and deposited onto a SiO_2 substrate. For the 30° homostructure, a single 30 nm WS_2 crystal was exfoliated onto a PPC/SiO_2 substrate and subsequently broken with the use of an AFM cantilever tip. Consecutive pick up of the two crystals with a 30° twist angle using a PMMA/PDMS membrane was followed by deposition onto another SiO_2 substrate. Thicknesses were measured with AFM.

Electron Beam Lithography: Samples were spin coated with ARP-9 resist (AllResist GmbH) at 3500 rpm for 60 s and baked at 180° for 5 min yielding a film of 200 nm thickness. EBL was performed in a Raith GmbH Voyager system operating at 50 kV using a beam current of 560 pA.

Reactive Ion Etching of TMDs and hBN: Anisotropic etching to imprint the resist pattern into the WS_2 crystals physically was carried out using a mixture of CHF_3 (14.5 sccm) and SF_6 (12.5 sccm) at a DC bias of 180 V and a pressure of 0.039 mbar for 40 s. Isotropic etching was achieved by using a more chemical recipe with solely SF_6 (30 sccm) at a DC bias of 40 V and a pressure of 0.13 mbar for 40 s. Removal of the remaining resist after etching was accomplished by a bath in warm 1165 resist remover (1 h) followed by Acetone (5 min) and IPA (5 min). If resist was still found on the sample, final cleaning was done in a bath of Acetone (1 h) and IPA (5 min) followed by 1 h in a UV ozone treatment. In some cases, the structures were slightly over-etched leading to nanoantennas with a small pedestal of SiO_2 (<20 nm) or gold (<5 nm). This, however, did not lead to any noticeable changes in the photonic resonances.

Reactive Ion Etching of GaS: Isotropic etching of GaS was achieved with $SiCl_4$ gas (5 sccm) at a pressure of 50 mTorr and DC bias of 175 V for 7 min. The resist removal step was the same as for other materials, however, this did not achieve proper removal of all resist from the sample. The residual resist did not noticeably impact the photonic resonances measured in dark field spectroscopy.

Gold Substrate Preparation: In order to prepare the gold substrate, a 10 nm layer of Ti was first deposited onto a 290 nm SiO_2/Si substrate via e-beam evaporation in order to improve the adhesion between substrate and gold. 130 nm of gold was subsequently deposited via the same method.

Dark Field Spectroscopy: Optical spectroscopy in a dark field configuration was achieved using a Nikon LV150N microscope with a fiber-coupled output. Incident illumination from a tungsten halogen lamp in the microscope was guided to a circular beam block with a diameter smaller than the beam diameter. The light was then reflected by a 45° tilted annular mirror toward a 50× Nikon (0.8 NA) dark-field objective which only illuminated the sample at large angles to the normal. Reflected light from the sample was guided back through the same objective toward a fiber coupler. Due to the small diameter of the multimode fiber core used, only light reflected back at small angles to the normal was collected. The fiber from the microscope was subsequently coupled to a Princeton Instruments spectrometer and charge coupled device.

FDTD Scattering Simulations: Calculations of the scattering cross section shown in Figures 4c and 5e and Notes S5 and S6, Supporting Information, were carried out by defining the geometry of the vdW material nanoantennas onto a SiO_2 or gold substrate utilizing the refractive indices extracted from the ellipsometry measurements. Illumination with a plane wave was sent normal to the surface using a TFSF source from the air side. The illumination was polarized parallel to the surface. The scattered intensity was subsequently collected from a monitor set above the illumination plane (in the far field) so that the dark field spectroscopy experiments could be closely emulated. The finite-difference time-domain simulations were carried out using Lumerical Inc. software.

Second Harmonic Generation: In order to probe the SHG signal from the twisted homostructures and their nanopillars, as shown in Figure 2d,f and Note S4, Supporting Information, we used a Mai-Tai Ti-sapphire mode-locked femtosecond laser as the excitation source set at 850 nm with an average power of 10 mW. The collimated laser light passed through a linear film polarizer, half wave plate, dichroic mirror and was incident on a 100× (0.7 NA) Mitutoyo objective which focused the excitation light onto the sample allowing us to probe single nanopillars and thin-film crystals. SHG light was then collected using the same objective subsequently reflecting the light from the dichroic mirror and passing it through an analyzer. The collected light was then filtered by long-pass filters (650 nm cutoff) and fiber coupled to a multi-mode fiber and sent to a Princeton Instruments spectrometer and CCD to yield the data displayed in Figure 2d,f as well as in Note S4, Supporting Information.

Third Harmonic Generation: THG measurements, shown in Figure 5, were carried out by illuminating the sample with 220 fs laser pulses (Yb:KGW Pharos, Light conversion) at 100 kHz repetition rate and a wavelength of 1500 nm through a 0.85 NA objective (60×). The laser beam was directed toward the sample via a dichroic mirror which transmitted the visible THG signal at 500 nm and reflected the illuminating wavelength. The illuminating beam was subsequently focused onto the back focal plane of the objective using a 1× telescope (100 mm) and the power was attenuated through a rotational neutral density wheel. The excitation power was measured with an infrared power meter (Thorlabs, S122C). The collected THG signal intensity from the sample was measured via a Thorlabs camera (CS165MUM) calibrated to convert counts/pixel to an intensity. The beam size of the THG signal and the excitation beam was measured by fitting the camera counts from a reference GaP sample emitting a strong second harmonic signal with a Gaussian function. The final peak intensity of the excitation and third harmonic signal was calculated by adjusting the power measurements with the respective beam sizes.

Nanoantenna THG resonances were recorded using a piezoelectric stage to scan the sample over the region of interest while the generated signal was recorded with a single-photon detector (Picoquant, Micro Photon Devices). The excitation wavelength ranged from 1240 to 1480 nm with increments of 40 nm using an excitation power of 6.5 μW. The reported THG intensity from each nanoantenna was determined using the counts of the single-photon detector and corrected with the beam size measurement so that excitation intensity fluctuations in this spectral range were taken into account.

Supporting Information

Supporting Information is available from the Wiley Online Library or from the author.

Acknowledgements

P.G.Z., T.S.M., S.R., X.H., and A.I.T. acknowledge support from the European Graphene Flagship Project under grant agreement number 881603 and EPSRC grants EP/S030751/1, EP/V006975/1, and EP/V026496/1. L.S. acknowledges funding support through a Humboldt Research Fellowship from the Alexander von Humboldt Foundation. Y.W. acknowledges a Research Fellowship (TOAST) awarded by the Royal Academy of Engineering. The authors would also like to thank Prof. Keith McKenna for his contribution concerning the enthalpy of formation factor in the etching speed of different vdW materials.

Conflict of Interest

The authors declare no conflict of interest.

Author Contributions

P.G.Z. and T.S.M. exfoliated WS_2, WSe_2, $MoSe_2$, MoS_2, $HfSe_2$, $ZrSe_2$ hBN, GaS, In_2Se_3, $MnPSe_3$, and $NiPS_3$ crystals onto SiO_2 substrates for ellipsometry measurements, nanoresonator fabrication, and THG susceptibility measurements. D.A.P. and M.B.G. performed ellipsometry measurements and fit the complex reflectance ratio with appropriate analytical models in order to extract the real and imaginary parts of the complex refractive index of each material. Y.W., X.H., and P.G.Z. fabricated nanoantenna structures using EBL and RIE. P.G.Z. performed SHG experiments to confirm the twist angle of the homostructures and their nanoantennas. P.G.Z., T.S.M., and S.R. performed all AFM characterization of crystal thickness and nanoantenna heights. P.G.Z., T.S.M., and S.R. performed all SEM measurements to characterize nanoantenna radii. P.G.Z., T.S.M., and S.R. recorded all dark field spectra and analyzed the results. C.L. and P.G.Z. fit the experimental and simulated scattering data to a coupled oscillator model to provide evidence of strong coupling and extract Rabi splittings. P.G.Z. and T.S.M. performed all FDTD simulations of the scattering cross sections. P.G.Z. and X.H. transferred WS_2 nanoantennas onto a monolayer WSe_2 crystal on a gold substrate. T.H. and S.V. performed THG experiments on WSe_2 nanoantennas as well as TMD thin-film crystals and subsequently analyzed the recorded spectra in order to extract $\chi^{(3)}$ values. T.F.K., B.D.G., R.S., and A.I.T. managed various aspects of the project. P.G.Z. and A.I.T. wrote the manuscript with contributions from all co-authors. P.G.Z., L.S., Y.W., and A.I.T. conceived the experiments and simulations. A.I.T. oversaw the entire project.

Data Availability Statement

The data that support the findings of this study are openly available in Figshare at https://doi.org/10.6084/m9.figshare.21397482, reference number 21397482.

Keywords

Mie resonators, nanophotonics, refractive index, third harmonic generation, transition metal dichalcogenides, van der Waals

Received: January 11, 2023
Revised: April 19, 2023
Published online:

[1] C. Jamois, R. B. Wehrspohn, L. C. Andreani, C. Hermann, O. Hess, U. Gösele, *Photonics Nanostruct. - Fundam. Appl.* **2003**, *1*, 1.
[2] B. Rigal, B. Dwir, A. Rudra, I. Kulkova, A. Lyasota, E. Kapon, *Appl. Phys. Lett.* **2018**, *112*, 051105.
[3] P. Lodahl, S. Mahmoodian, S. Stobbe, *Rev. Mod. Phys.* **2015**, *87*, 347.
[4] J. Cambiasso, G. Grinblat, Y. Li, A. Rakovich, E. Cortés, S. A. Maier, *Nano Lett.* **2017**, *17*, 1219.
[5] F. Liu, A. J. Brash, J. O'Hara, L. M. Martins, C. L. Phillips, R. J. Coles, B. Royall, E. Clarke, C. Bentham, N. Prtljaga, I. E. Itskevich, L. R. Wilson, M. S. Skolnick, A. M. Fox, *Nat. Nanotechnol.* **2018**, *13*, 835.
[6] L. Sortino, P. G. Zotev, S. Mignuzzi, J. Cambiasso, D. Schmidt, A. Genco, M. Aßmann, M. Bayer, S. A. Maier, R. Sapienza, A. I. Tartakovskii, *Nat. Commun.* **2019**, *10*, 5119.
[7] S. Wu, S. Buckley, J. R. Schaibley, L. Feng, J. Yan, D. G. Mandrus, F. Hatami, W. Yao, J. Vučković, A. Majumdar, X. Xu, *Nature* **2015**, *520*, 69.
[8] G. Grinblat, Y. Li, M. P. Nielsen, R. F. Oulton, S. A. Maier, *ACS Nano* **2017**, *11*, 953.
[9] R. Chikkaraddy, B. De Nijs, F. Benz, S. J. Barrow, O. A. Scherman, E. Rosta, A. Demetriadou, P. Fox, O. Hess, J. J. Baumberg, *Nature* **2016**, *535*, 127.
[10] D. G. Baranov, M. Wersäll, J. Cuadra, T. J. Antosiewicz, T. Shegai, *ACS Photonics* **2018**, *5*, 24.
[11] K. Wang, E. Schonbrun, P. Steinvurzel, K. B. Crozier, *Nat. Commun.* **2011**, *2*, 469.

[12] Z. Xu, W. Song, K. B. Crozier, *ACS Photonics* **2018**, *5*, 4993.
[13] D. Conteduca, G. Brunetti, G. Pitruzzello, F. Tragni, K. Dholakia, T. F. Krauss, C. Ciminelli, *ACS Photonics* **2021**, *8*, 2060.
[14] G. M. Akselrod, C. Argyropoulos, T. B. Hoang, C. Ciracì, C. Fang, J. Huang, D. R. Smith, M. H. Mikkelsen, *Nat. Photonics* **2014**, *8*, 835.
[15] M. Blauth, M. Jürgensen, G. Vest, O. Hartwig, M. Prechtl, J. Cerne, J. J. Finley, M. Kaniber, *Nano Lett.* **2018**, *18*, 6812.
[16] Y. Luo, G. D. Shepard, J. V. Ardelean, D. A. Rhodes, B. Kim, K. Barmak, J. C. Hone, S. Strauf, *Nat. Nanotechnol.* **2018**, *13*, 1137.
[17] J. B. Khurgin, *Nat. Nanotechnol.* **2015**, *10*, 2.
[18] R. M. Bakker, D. Permyakov, Y. F. Yu, D. Markovich, R. Paniagua-Domínguez, L. Gonzaga, A. Samusev, Y. Kivshar, B. Lukyanchuk, A. I. Kuznetsov, *Nano Lett.* **2015**, *15*, 2137.
[19] D. G. Baranov, D. A. Zuev, S. I. Lepeshov, O. V. Kotov, A. E. Krasnok, A. B. Evlyukhin, B. N. Chichkov, *Optica* **2017**, *4*, 814.
[20] R. Verre, D. G. Baranov, B. Munkhbat, J. Cuadra, M. Käll, T. Shegai, *Nat. Nanotechnol.* **2019**, *14*, 679.
[21] T. S. Moss, *Phys. Status Solidi B* **1985**, *131*, 415.
[22] B. Munkhbat, P. Wróbel, T. J. Antosiewicz, T. O. Shegai, *ACS Photonics* **2022**, *9*, 2398.
[23] Y. Rah, Y. Jin, S. Kim, K. Yu, *Opt. Lett.* **2019**, *44*, 3797.
[24] Y. Liu, Y. Huang, X. Duan, *Nature* **2019**, *567*, 323.
[25] Y. Yang, O. D. Miller, T. Christensen, J. D. Joannopoulos, M. Soljačić, *Nano Lett.* **2017**, *17*, 3238.
[26] K. Yao, N. R. Finney, J. Zhang, S. L. Moore, L. Xian, N. Tancogne-Dejean, F. Liu, J. Ardelean, X. Xu, D. Halbertal, K. Watanabe, T. Taniguchi, H. Ochoa, A. Asenjo-Garcia, X. Zhu, D. N. Basov, A. Rubio, C. R. Dean, J. Hone, P. J. Schuck, *Sci. Adv.* **2021**, *7*, eabe8691.
[27] A. K. Geim, I. V. Grigorieva, *Nature* **2013**, *499*, 419.
[28] Y. Liu, N. O. Weiss, X. Duan, H. C. Cheng, Y. Huang, X. Duan, *Nat. Rev. Mater.* **2016**, *1*, 9.
[29] Y. Liu, C. Zeng, J. Yu, J. Zhong, B. Li, Z. Zhang, Z. Liu, Z. M. Wang, A. Pan, X. Duan, *Chem. Soc. Rev.* **2021**, *50*, 6401.
[30] P. G. Zotev, Y. Wang, L. Sortino, T. S. Millard, N. Mullin, D. Conteduca, M. Shagar, A. Genco, J. K. Hobbs, T. F. Krauss, A. I. Tartakovskii, *ACS Nano* **2022**, *16*, 6493.
[31] J. D. Caldwell, *Nat. Rev. Mater.* **2019**, *4*, 552.
[32] S. Busschaert, M. Cavigelli, R. Khelifa, A. Jain, L. Novotny, *ACS Photonics* **2020**, *7*, 2482.
[33] X. Zhang, X. Zhang, W. Huang, K. Wu, M. Zhao, A. T. Charlie Johnson, S. Tongay, E. Cubukcu, *Adv. Opt. Mater.* **2020**, *8*, 1901988.
[34] B. Munkhbat, B. Küçüköz, D. G. Baranov, T. J. Antosiewicz, T. O. Shegai, *Laser Photonics Rev.* **2022**, *17*, 2200057.
[35] M. Qin, J. Duan, S. Xiao, W. Liu, T. Yu, T. Wang, Q. Liao, *Phys. Rev. B* **2023**, *107*, 045417.
[36] T. Weber, L. Sortino, A. B. Mhenni, N. P. Wilson, J. J. Finley, S. A. Maier, A. Tittl, *arXiv:2209.01944*, **2022**.
[37] M. Nauman, J. Yan, D. de Ceglia, M. Rahmani, K. Zangeneh Kamali, C. De Angelis, A. E. Miroshnichenko, Y. Lu, D. N. Neshev, *Nat. Commun.* **2021**, *12*, 5597.
[38] H. Zhang, B. Abhiraman, Q. Zhang, J. Miao, K. Jo, S. Roccasecca, M. W. Knight, A. R. Davoyan, D. Jariwala, *Nat. Commun.* **2020**, *11*, 3552.
[39] G. A. Ermolaev, D. V. Grudinin, Y. V. Stebunov, V. G. Kravets, J. Duan, G. I. Tselikov, K. V. Voronin, D. I. Yakubovsky, S. M. Novikov, D. G. Baranov, A. Y. Nikitin, T. Shegai, P. Alonso-González, A. N. Grigorenko, A. V. Arsenin, K. S. Novoselov, V. S. Volkov, *Nat. Commun.* **2021**, *12*, 854.
[40] A. Popkova, I. Antropov, G. I. Tselikov, G. A. Ermolaev, I. Ozerov, R. V. Kirtaev, S. M. Novikov, A. B. Evlyukhin, A. V. Arsening, V. O. Bessonov, V. S. Volkov, A. A. Fedyanin, *Laser Photonics Rev.* **2022**, *16*, 2100604.
[41] X. Xu, C. Trovatello, F. Mooshammer, Y. Shao, S. Zhang, K. Yao, D. N. Basov, G. Cerullo, P. J. Schuck, *Nat. Photonics* **2022**, *16*, 698.
[42] N. Muhammad, Y. Chen, C. W. Qiu, G. P. Wang, *Nano Lett.* **2021**, *21*, 967.
[43] H. Ling, R. Li, A. R. Davoyan, *ACS Photonics* **2021**, *8*, 721.
[44] Y. Li, A. Chernikov, X. Zhang, A. Rigosi, H. M. Hill, A. M. V. D. Zande, D. A. Chenet, E.-m. Shih, J. Hone, T. F. Heinz, *Phys. Rev. B* **2014**, *90*, 205422.
[45] K. Kato, N. Umemura, *Opt. Lett.* **2011**, *36*, 746.
[46] A. Segura, L. Artús, R. Cuscó, T. Taniguchi, G. Cassabois, B. Gil, *Phys. Rev. Mater.* **2018**, *2*, 024001.
[47] Y. Cho, S. M. Anderson, B. S. Mendoza, S. Okano, R. Carriles, N. Arzate, A. I. Shkrebtii, D. Wu, K. Lai, D. R. T. Zahn, M. C. Downer, *arXiv:1911.01784*, **2019**.
[48] S. Y. Kim, T. Y. Kim, L. J. Sandilands, S. Sinn, M. C. Lee, J. Son, S. Lee, K. Y. Choi, W. Kim, B. G. Park, C. Jeon, H. D. Kim, C. H. Park, J. G. Park, S. J. Moon, T. W. Noh, *Phys. Rev. Lett.* **2018**, *120*, 136402.
[49] H. N. Jaiswal, M. Liu, S. Shahi, F. Yao, Q. Zhao, X. Xu, H. Li, *Semicond. Sci. Technol.* **2018**, *33*, 124014.
[50] C. Lane, J. X. Zhu, *Phys. Rev. B* **2020**, *102*, 075124.
[51] B. Munkhbat, A. B. Yankovich, D. G. Baranov, R. Verre, E. Olsson, S. Timur, *Nat. Commun.* **2020**, *11*, 4604.
[52] D. R. Danielsen, A. Lyksborg-Andersen, K. E. Nielsen, B. S. Jessen, T. J. Booth, M. H. Doan, Y. Zhou, P. Bøggild, L. Gammelgaard, *ACS Appl. Mater. Interfaces* **2021**, *13*, 41886.
[53] S. Chen, Y. Pan, D. Wang, H. Deng, *J. Electron. Mater.* **2020**, *49*, 7363.
[54] P. A. O'Hare, B. M. Lewis, B. A. Parkinson, *J. Chem. Thermodyn.* **1988**, *20*, 681.
[55] P. A. O'Hare, I. R. Tasker, J. M. Tarascon, *J. Chem. Thermodyn.* **1987**, *19*, 61.
[56] D. S. Dovzhenko, S. V. Ryabchuk, Y. P. Rakovich, I. R. Nabiev, *Nanoscale* **2018**, *10*, 3589.
[57] S. Shen, Y. Wu, Y. Li, P. Xie, Q. Ding, X. Kuang, W. Wang, W. Wang, *Phys. Rev. B* **2022**, *105*, 155403.
[58] H. L. Liu, T. Yang, J. H. Chen, H. W. Chen, H. Guo, R. Saito, M. Y. Li, L. J. Li, *Sci. Rep.* **2020**, *10*, 15282.
[59] Q. Ren, J. Lu, H. H. Tan, S. Wu, L. Sun, W. Zhou, W. Xie, Z. Sun, Y. Zhu, C. Jagadish, S. C. Shen, Z. Chen, *Nano Lett.* **2012**, *12*, 3455.
[60] A. E. Miroshnichenko, A. B. Evlyukhin, Y. F. Yu, R. M. Bakker, A. Chipouline, A. I. Kuznetsov, B. Luk'yanchuk, B. N. Chichkov, Y. S. Kivshar, *Nat. Commun.* **2015**, *6*, 8069.
[61] M. Timofeeva, L. Lang, F. Timpu, C. Renaut, A. Bouravleuv, I. Shtrom, G. Cirlin, R. Grange, *Nano Lett.* **2018**, *18*, 3695.
[62] C. H. Liu, J. Zheng, S. Colburn, T. K. Fryett, Y. Chen, X. Xu, A. Majumdar, *Nano Lett.* **2018**, *18*, 6961.
[63] K. O'Brien, H. Suchowski, J. Rho, A. Salandrino, B. Kante, X. Yin, X. Zhang, *Nat. Mater.* **2015**, *14*, 379.
[64] Y. Wang, F. Iyikanat, H. Rostami, X. Bai, X. Hu, S. Das, Y. Dai, L. Du, Y. Zhang, S. Li, H. Lipsanen, F. J. García de Abajo, Z. Sun, *Adv. Mater.* **2022**, *34*, 2107104.
[65] H. G. Rosa, Y. W. Ho, I. Verzhbitskiy, M. J. Rodrigues, T. Taniguchi, K. Watanabe, G. Eda, V. M. Pereira, J. C. Gomes, *Sci. Rep.* **2018**, *8*, 10035.
[66] R. Zhou, A. Krasnok, N. Hussain, S. Yang, K. Ullah, *Nanophotonics* **2022**, *11*, 3007.
[67] A. Penzkofer, P. Qiu, F. Ossig, N. F. H-physik, U. Regensburg, A. Sinica, P. Rep, in *Nonlinear Optics of Organics and Semiconductors*, Springer Proceedings in Physics, Vol. *36*, Springer Berlin, Heidelberg **1989**, pp. 312–320.
[68] D. E. Aspnes, A. A. Studna, *Phys. Rev. B* **1983**, *27*, 985.
[69] D. X. Nguyen, X. Letartre, E. Drouard, P. Viktorovitch, H. C. Nguyen, H. S. Nguyen, *Phys. Rev. Res.* **2022**, *4*, L032031.
[70] S. Dufferwiel, T. P. Lyons, D. D. Solnyshkov, A. A. P. Trichet, F. Withers, G. Malpuech, J. M. Smith, K. S. Novoselov, M. S. Skolnick, D. N. Krizhanovskii, A. I. Tartakovskii, *Nat. Commun.* **2018**, *9*, 4797.

[71] D. J. Gillard, A. Genco, S. Ahn, T. P. Lyons, K. Yeol Ma, A. R. Jang, T. Severs Millard, A. A. Trichet, R. Jayaprakash, K. Georgiou, D. G. Lidzey, J. M. Smith, H. Suk Shin, A. I. Tartakovskii, *2D Mater.* **2021**, *8*, 011002.
[72] M. S. Skolnick, T. A. Fisher, D. M. Whittaker, *Semicond. Sci. Technol.* **1998**, *13*, 645.
[73] V. Savona, L. C. Andreani, P. Schwendimann, A. Quattropani, *Solid State Commun.* **1995**, *93*, 733.
[74] H. Suchomel, S. Kreutzer, M. Jörg, S. Brodbeck, M. Pieczarka, S. Betzold, C. P. Dietrich, G. Sęk, C. Schneider, S. Höfling, *Opt. Express* **2017**, *25*, 24816.
[75] G. Christmann, R. Butté, E. Feltin, A. Mouti, P. A. Stadelmann, A. Castiglia, J. F. Carlin, N. Grandjean, *Phys. Rev. B: Condens. Matter Mater. Phys.* **2008**, *77*, 085310.
[76] F. A. Bovino, M. Giardina, M. C. Larciprete, A. Belardini, M. Centini, C. Sibilia, M. Bertolotti, A. Passaseo, V. Tasco, *Opt. Express* **2009**, *17*, 19337.